10-2007

Upper limit map of a background of gravitational waves

B. P. Abbott

R. Abbott

Mario C. Diaz
The University of Texas Rio Grande Valley

R. Grosso

Soumya Mohanty
The University of Texas Rio Grande Valley

See next page for additional authors

Authors

B. P. Abbott, R. Abbott, Mario C. Diaz, R. Grosso, Soumya Mohanty, Soma Mukherjee, and Cristina V. Torres

Upper limit map of a background of gravitational waves

B. Abbott,[14] R. Abbott,[14] R. Adhikari,[14] J. Agresti,[14] P. Ajith,[2] B. Allen,[2,51] R. Amin,[18] S. B. Anderson,[14]
W. G. Anderson,[51] M. Arain,[39] M. Araya,[14] H. Armandula,[14] M. Ashley,[4] S. Aston,[38] P. Aufmuth,[36] C. Aulbert,[1] S. Babak,[1]
S. Ballmer,[14] H. Bantilan,[8] B. C. Barish,[14] C. Barker,[15] D. Barker,[15] B. Barr,[40] P. Barriga,[50] M. A. Barton,[40] K. Bayer,[17]
K. Belczynski,[24] J. Betzwieser,[17] P. T. Beyersdorf,[27] B. Bhawal,[14] I. A. Bilenko,[21] G. Billingsley,[14] R. Biswas,[51]
E. Black,[14] K. Blackburn,[14] L. Blackburn,[17] D. Blair,[50] B. Bland,[15] J. Bogenstahl,[40] L. Bogue,[16] R. Bork,[14] V. Boschi,[14]
S. Bose,[52] P. R. Brady,[51] V. B. Braginsky,[21] J. E. Brau,[43] M. Brinkmann,[2] A. Brooks,[37] D. A. Brown,[14,6] A. Bullington,[30]
A. Bunkowski,[2] A. Buonanno,[41] O. Burmeister,[2] D. Busby,[14] R. L. Byer,[30] L. Cadonati,[17] G. Cagnoli,[40] J. B. Camp,[22]
J. Cannizzo,[22] K. Cannon,[51] C. A. Cantley,[40] J. Cao,[17] L. Cardenas,[14] M. M. Casey,[40] G. Castaldi,[46] C. Cepeda,[14]
E. Chalkey,[40] P. Charlton,[9] S. Chatterji,[14] S. Chelkowski,[2] Y. Chen,[1] F. Chiadini,[45] D. Chin,[42] E. Chin,[50] J. Chow,[4]
N. Christensen,[8] J. Clark,[40] P. Cochrane,[2] T. Cokelaer,[7] C. N. Colacino,[38] R. Coldwell,[39] R. Conte,[45] D. Cook,[15]
T. Corbitt,[17] D. Coward,[50] D. Coyne,[14] J. D. E. Creighton,[51] T. D. Creighton,[14] R. P. Croce,[46] D. R. M. Crooks,[40]
A. M. Cruise,[38] A. Cumming,[40] J. Dalrymple,[31] E. D'Ambrosio,[14] K. Danzmann,[36,2] G. Davies,[7] D. DeBra,[30]
J. Degallaix,[50] M. Degree,[30] T. Demma,[46] V. Dergachev,[42] S. Desai,[32] R. DeSalvo,[14] S. Dhurandhar,[13] M. Díaz,[33]
J. Dickson,[4] A. Di Credico,[31] G. Diederichs,[36] A. Dietz,[7] E. E. Doomes,[29] R. W. P. Drever,[5] J.-C. Dumas,[50] R. J. Dupuis,[14]
J. G. Dwyer,[10] P. Ehrens,[14] E. Espinoza,[14] T. Etzel,[14] M. Evans,[14] T. Evans,[16] S. Fairhurst,[7,14] Y. Fan,[50] D. Fazi,[14]
M. M. Fejer,[30] L. S. Finn,[32] V. Fiumara,[45] N. Fotopoulos,[51] A. Franzen,[36] K. Y. Franzen,[39] A. Freise,[38] R. Frey,[43]
T. Fricke,[44] P. Fritschel,[17] V. V. Frolov,[16] M. Fyffe,[16] V. Galdi,[46] J. Garofoli,[15] I. Gholami,[1] J. A. Giaime,[16,18]
S. Giampanis,[44] K. D. Giardina,[16] K. Goda,[17] E. Goetz,[42] L. M. Goggin,[14] G. González,[18] S. Gossler,[4] A. Grant,[40]
S. Gras,[50] C. Gray,[15] M. Gray,[4] J. Greenhalgh,[26] A. M. Gretarsson,[11] R. Grosso,[33] H. Grote,[2] S. Grunewald,[1]
M. Guenther,[15] R. Gustafson,[42] B. Hage,[36] D. Hammer,[51] C. Hanna,[18] J. Hanson,[16] J. Harms,[2] G. Harry,[17] E. Harstad,[43]
T. Hayler,[26] J. Heefner,[14] I. S. Heng,[40] A. Heptonstall,[40] M. Heurs,[2] M. Hewitson,[2] S. Hild,[36] E. Hirose,[31] D. Hoak,[16]
D. Hosken,[37] J. Hough,[40] E. Howell,[50] D. Hoyland,[38] S. H. Huttner,[40] D. Ingram,[15] E. Innerhofer,[17] M. Ito,[43] Y. Itoh,[51]
A. Ivanov,[14] D. Jackrel,[30] B. Johnson,[15] W. W. Johnson,[18] D. I. Jones,[47] G. Jones,[7] R. Jones,[40] L. Ju,[50] P. Kalmus,[10]
V. Kalogera,[24] D. Kasprzyk,[38] E. Katsavounidis,[17] K. Kawabe,[15] S. Kawamura,[23] F. Kawazoe,[23] W. Kells,[14]
D. G. Keppel,[14] F. Ya. Khalili,[21] C. Kim,[24] P. King,[14] J. S. Kissel,[18] S. Klimenko,[39] K. Kokeyama,[23] V. Kondrashov,[14]
R. K. Kopparapu,[18] D. Kozak,[14] B. Krishnan,[1] P. Kwee,[36] P. K. Lam,[4] M. Landry,[15] B. Lantz,[30] A. Lazzarini,[14] B. Lee,[50]
M. Lei,[14] J. Leiner,[52] V. Leonhardt,[23] I. Leonor,[43] K. Libbrecht,[14] P. Lindquist,[14] N. A. Lockerbie,[48] M. Longo,[45]
M. Lormand,[16] M. Lubinski,[15] H. Lück,[2,36] B. Machenschalk,[1] M. MacInnis,[17] M. Mageswaran,[14] K. Mailand,[14]
M. Malec,[36] V. Mandic,[14] S. Marano,[45] S. Márka,[10] J. Markowitz,[17] E. Maros,[14] I. Martin,[40] J. N. Marx,[14] K. Mason,[17]
L. Matone,[10] V. Matta,[45] N. Mavalvala,[17] R. McCarthy,[15] D. E. McClelland,[4] S. C. McGuire,[29] M. McHugh,[20]
K. McKenzie,[4] J. W. C. McNabb,[32] S. McWilliams,[22] T. Meier,[36] A. Melissinos,[44] G. Mendell,[15] R. A. Mercer,[39]
S. Meshkov,[14] E. Messaritaki,[14] C. J. Messenger,[40] D. Meyers,[14] E. Mikhailov,[17] S. Mitra,[13] V. P. Mitrofanov,[21]
G. Mitselmakher,[39] R. Mittleman,[17] O. Miyakawa,[14] S. Mohanty,[33] G. Moreno,[15] K. Mossavi,[2] C. MowLowry,[4]
A. Moylan,[4] D. Mudge,[37] G. Mueller,[39] S. Mukherjee,[33] H. Müller-Ebhardt,[2] J. Munch,[37] P. Murray,[40] E. Myers,[15]
J. Myers,[15] G. Newton,[40] A. Nishizawa,[23] K. Numata,[22] B. O'Reilly,[16] R. O'Shaughnessy,[24] D. J. Ottaway,[17]
H. Overmier,[16] B. J. Owen,[32] Y. Pan,[41] M. A. Papa,[1,51] V. Parameshwaraiah,[15] P. Patel,[14] M. Pedraza,[14] S. Penn,[12]
V. Pierro,[46] I. M. Pinto,[46] M. Pitkin,[40] H. Pletsch,[2] M. V. Plissi,[40] F. Postiglione,[45] R. Prix,[1] V. Quetschke,[39] F. Raab,[15]
D. Rabeling,[4] H. Radkins,[15] R. Rahkola,[43] N. Rainer,[2] M. Rakhmanov,[32] K. Rawlins,[17] S. Ray-Majumder,[51] V. Re,[38]
H. Rehbein,[2] S. Reid,[40] D. H. Reitze,[39] L. Ribichini,[2] R. Riesen,[16] K. Riles,[42] B. Rivera,[15] N. A. Robertson,[14,40]
C. Robinson,[7] E. L. Robinson,[38] S. Roddy,[16] A. Rodriguez,[18] A. M. Rogan,[52] J. Rollins,[10] J. D. Romano,[7] J. Romie,[16]
R. Route,[30] S. Rowan,[40] A. Rüdiger,[2] L. Ruet,[17] P. Russell,[14] K. Ryan,[15] S. Sakata,[23] M. Samidi,[14]
L. Sancho de la Jordana,[35] V. Sandberg,[15] V. Sannibale,[14] S. Saraf,[25] P. Sarin,[17] B. S. Sathyaprakash,[7] S. Sato,[23]
P. R. Saulson,[31] R. Savage,[15] P. Savov,[6] S. Schediwy,[50] R. Schilling,[2] R. Schnabel,[2] R. Schofield,[43] B. F. Schutz,[1,7]
P. Schwinberg,[15] S. M. Scott,[4] A. C. Searle,[4] B. Sears,[14] F. Seifert,[2] D. Sellers,[16] A. S. Sengupta,[7] P. Shawhan,[41]
D. H. Shoemaker,[17] A. Sibley,[16] J. A. Sidles,[49] X. Siemens,[6,14] D. Sigg,[15] S. Sinha,[30] A. M. Sintes,[1,35] B. J. J. Slagmolen,[4]
J. Slutsky,[18] J. R. Smith,[2] M. R. Smith,[14] K. Somiya,[2,1] K. A. Strain,[40] D. M. Strom,[43] A. Stuver,[32] T. Z. Summerscales,[3]
K.-X. Sun,[30] M. Sung,[18] P. J. Sutton,[14] H. Takahashi,[1] D. B. Tanner,[39] M. Tarallo,[14] R. Taylor,[14] R. Taylor,[40] J. Thacker,[16]
K. A. Thorne,[32] K. S. Thorne,[6] A. Thüring,[36] K. V. Tokmakov,[40] C. Torres,[33] C. Torrie,[40] G. Traylor,[16] M. Trias,[35]
W. Tyler,[14] D. Ugolini,[34] C. Ungarelli,[38] K. Urbanek,[30] H. Vahlbruch,[36] M. Vallisneri,[6] C. Van Den Broeck,[7] M. Varvella,[14]

S. Vass,[14] A. Vecchio,[38] J. Veitch,[40] P. Veitch,[37] A. Villar,[14] C. Vorvick,[15] S. P. Vyachanin,[21] S. J. Waldman,[14] L. Wallace,[14] H. Ward,[40] R. Ward,[14] K. Watts,[16] D. Webber,[14] A. Weidner,[2] M. Weinert,[2] A. Weinstein,[14] R. Weiss,[17] S. Wen,[18] K. Wette,[4] J. T. Whelan,[1] D. M. Whitbeck,[32] S. E. Whitcomb,[14] B. F. Whiting,[39] C. Wilkinson,[15] P. A. Willems,[14] L. Williams,[39] B. Willke,[2,36] I. Wilmut,[26] W. Winkler,[2] C. C. Wipf,[17] S. Wise,[39] A. G. Wiseman,[51] G. Woan,[40] D. Woods,[51] R. Wooley,[16] J. Worden,[15] W. Wu,[39] I. Yakushin,[16] H. Yamamoto,[14] Z. Yan,[50] S. Yoshida,[28] N. Yunes,[32] M. Zanolin,[17] J. Zhang,[42] L. Zhang,[14] C. Zhao,[50] N. Zotov,[19] M. Zucker,[17] H. zur Mühlen,[36] and J. Zweizig[14]

(LIGO Scientific Collaboration)

[1]*Albert-Einstein-Institut, Max-Planck-Institut für Gravitationsphysik, D-14476 Golm, Germany*
[2]*Albert-Einstein-Institut, Max-Planck-Institut für Gravitationsphysik, D-30167 Hannover, Germany*
[3]*Andrews University, Berrien Springs, Michigan 49104 USA*
[4]*Australian National University, Canberra, 0200, Australia*
[5]*California Institute of Technology, Pasadena, California 91125, USA*
[6]*Caltech-CaRT, Pasadena, California 91125, USA*
[7]*Cardiff University, Cardiff, CF2 3YB, United Kingdom*
[8]*Carleton College, Northfield, Minnesota 55057, USA*
[9]*Charles Sturt University, Wagga Wagga, NSW 2678, Australia*
[10]*Columbia University, New York, New York 10027, USA*
[11]*Embry-Riddle Aeronautical University, Prescott, Arizona 86301 USA*
[12]*Hobart and William Smith Colleges, Geneva, New York 14456, USA*
[13]*Inter-University Centre for Astronomy and Astrophysics, Pune - 411007, India*
[14]*LIGO–California Institute of Technology, Pasadena, California 91125, USA*
[15]*LIGO Hanford Observatory, Richland, Washington 99352, USA*
[16]*LIGO Livingston Observatory, Livingston, Louisiana 70754, USA*
[17]*LIGO–Massachusetts Institute of Technology, Cambridge, Massachusetts 02139, USA*
[18]*Louisiana State University, Baton Rouge, Louisiana 70803, USA*
[19]*Louisiana Tech University, Ruston, Louisiana 71272, USA*
[20]*Loyola University, New Orleans, Louisiana 70118, USA*
[21]*Moscow State University, Moscow, 119992, Russia*
[22]*NASA/Goddard Space Flight Center, Greenbelt, Maryland 20771, USA*
[23]*National Astronomical Observatory of Japan, Tokyo 181-8588, Japan*
[24]*Northwestern University, Evanston, Illinois 60208, USA*
[25]*Rochester Institute of Technology, Rochester, New York 14623, USA*
[26]*Rutherford Appleton Laboratory, Chilton, Didcot, Oxon OX11 0QX United Kingdom*
[27]*San Jose State University, San Jose, California 95192, USA*
[28]*Southeastern Louisiana University, Hammond, Louisiana 70402, USA*
[29]*Southern University and A&M College, Baton Rouge, Louisiana 70813, USA*
[30]*Stanford University, Stanford, California 94305, USA*
[31]*Syracuse University, Syracuse, New York 13244, USA*
[32]*The Pennsylvania State University, University Park, Pennsylvania 16802, USA*
[33]*The University of Texas at Brownsville and Texas Southmost College, Brownsville, Texas 78520, USA*
[34]*Trinity University, San Antonio, Texas 78212, USA*
[35]*Universitat de les Illes Balears, E-07122 Palma de Mallorca, Spain*
[36]*Universität Hannover, D-30167 Hannover, Germany*
[37]*University of Adelaide, Adelaide, SA 5005, Australia*
[38]*University of Birmingham, Birmingham, B15 2TT, United Kingdom*
[39]*University of Florida, Gainesville, Florida 32611, USA*
[40]*University of Glasgow, Glasgow, G12 8QQ, United Kingdom*
[41]*University of Maryland, College Park, Maryland 20742 USA*
[42]*University of Michigan, Ann Arbor, Michigan 48109, USA*
[43]*University of Oregon, Eugene, Oregon 97403, USA*
[44]*University of Rochester, Rochester, New York 14627, USA*
[45]*University of Salerno, 84084 Fisciano (Salerno), Italy*
[46]*University of Sannio at Benevento, I-82100 Benevento, Italy*
[47]*University of Southampton, Southampton, SO17 1BJ, United Kingdom*
[48]*University of Strathclyde, Glasgow, G1 1XQ, United Kingdom*
[49]*University of Washington, Seattle, Washington, 98195, USA*
[50]*University of Western Australia, Crawley, WA 6009, Australia*

^{51}*University of Wisconsin-Milwaukee, Milwaukee, Wisconsin 53201, USA*
^{52}*Washington State University, Pullman, Washington 99164, USA*

We searched for an anisotropic background of gravitational waves using data from the LIGO S4 science run and a method that is optimized for point sources. This is appropriate if, for example, the gravitational wave background is dominated by a small number of distinct astrophysical sources. No signal was seen. Upper limit maps were produced assuming two different power laws for the source strain power spectrum. For an f^{-3} power law and using the 50 Hz to 1.8 kHz band the upper limits on the source strain power spectrum vary between 1.2×10^{-48} Hz^{-1} $(100$ Hz$/f)^3$ and 1.2×10^{-47} Hz^{-1} $(100$ Hz$/f)^3$, depending on the position in the sky. Similarly, in the case of constant strain power spectrum, the upper limits vary between 8.5×10^{-49} Hz^{-1} and 6.1×10^{-48} Hz^{-1}. As a side product a limit on an isotropic background of gravitational waves was also obtained. All limits are at the 90% confidence level. Finally, as an application, we focused on the direction of Sco-X1, the brightest low-mass x-ray binary. We compare the upper limit on strain amplitude obtained by this method to expectations based on the x-ray flux from Sco-X1.

I. INTRODUCTION

A stochastic background of gravitational waves can be anisotropic if, for example, the dominant source of stochastic gravitational waves comes from an ensemble of astrophysical sources (e.g., [1,2]), and if this ensemble is dominated by its strongest members. So far the LIGO Scientific Collaboration has analyzed the data from the first science runs for a stochastic background of gravitational waves [3–5], assuming that this background is *isotropic*. If astrophysical sources indeed dominate this background, one should look for anisotropies.

A method that is optimized for extreme anisotropies, namely, point sources of stochastic gravitational radiation, was presented in [6]. It is based on the cross correlation of the data streams from two spatially separated gravitational wave interferometers, and is referred to as the radiometer analysis. We have analyzed the data of the 4th LIGO science run using this method.

Section II is a short description of the radiometer analysis method. The peculiarities of the S4 science run are summarized in Sec. III, and we discuss the results in Sec. IV.

II. METHOD DESCRIPTION

A stochastic background of gravitational waves can be distinguished from other sources of detector noise by cross correlating two independent detectors. Thus we cross correlate the data streams from a pair of detectors with a cross correlation kernel Q, chosen to be optimal for a source which is specified by an assumed strain power spectrum $H(f)$ and angular power distribution $P(\hat{\Omega})$. Specifically, with the data stream divided into intervals labeled by t, and with $\tilde{s}_{1,t}(f)$ and $\tilde{s}_{2,t}(f)$ representing the Fourier transforms of the strain outputs of two detectors, this cross correlation is computed in the frequency domain interval by interval as

$$Y_t = \int_{-\infty}^{\infty} df\, \tilde{s}_{1,t}{}^*(f) Q_t(f) \tilde{s}_{2,t}(f). \tag{1}$$

In contrast to the isotropic analysis the optimal filter Q_t is now sidereal time dependent. It has the general form

$$Q_t(f) = \lambda_t \frac{\int_{S^2} d\hat{\Omega}\, \gamma_{\hat{\Omega},t}(f) P(\hat{\Omega}) H(|f|)}{P_1(f) P_2(f)} \tag{2}$$

where λ_t is a normalization factor, P_1 and P_2 are the strain noise power spectra of the two detectors. $H(|f|)$ and $P(\hat{\Omega})$ are defined by

$$\langle h^*_{Af\hat{\Omega}} h_{A'f'\hat{\Omega}'} \rangle = \delta_{AA'}\delta(f - f')\delta^2(\hat{\Omega}, \hat{\Omega}') P(\hat{\Omega}) \frac{H(|f|)}{4} \tag{3}$$

where $H(|f|)$ is the one-sided (positive frequencies only) spectrum of strain power, summed over both polarizations. This explains the factor of $\frac{1}{4}$ and is appropriate for the unpolarized stochastic background we search for. $h_{Af\hat{\Omega}}$ is the gravitational wave strain in polarization A at frequency f arriving from the direction $\hat{\Omega}$. Finally, the factor $\gamma_{\hat{\Omega},t}$ in Eq. (2) takes into account the sidereal time dependent time delay due to the detector separation and the directionality of the acceptance of the detector pair. Assuming that the source is unpolarized, $\gamma_{\hat{\Omega},t}$ is given by

$$\gamma_{\hat{\Omega},t}(f) = \frac{1}{2} \sum_A e^{i2\pi f \hat{\Omega} \cdot \Delta \vec{x}_t/c} F_{1,t}{}^A(\hat{\Omega}) F_{2,t}{}^A(\hat{\Omega}) \tag{4}$$

where $\Delta \vec{x}_t = \vec{x}_{2,t} - \vec{x}_{1,t}$ is the detector separation vector, $\hat{\Omega}$ is the unit vector specifying the sky position, and

$$F_{i,t}{}^A(\hat{\Omega}) = e^A_{ab}(\hat{\Omega})\tfrac{1}{2}(\hat{X}_{i,t}{}^a \hat{X}_{i,t}{}^b - \hat{Y}_{i,t}{}^a \hat{Y}_{i,t}{}^b) \tag{5}$$

is the response of detector i to a zero frequency, unit amplitude, $A = +$ or $\times$ polarized gravitational wave. $e^A_{ab}(\hat{\Omega})$ is the spin-two polarization tensor for polarization

A and $\hat{X}_{i,t}{}^a$ and $\hat{Y}_{i,t}{}^a$ are unit vectors pointing in the directions of the detector arms (see [7] for details). The sidereal time dependence enters through the rotation of the earth, affecting $\hat{X}_{i,t}{}^a$, $\hat{Y}_{i,t}{}^a$, and $\Delta \vec{x}_t$.

The optimal filter Q_t is derived assuming that the intrinsic detector noise is Gaussian and stationary over the measurement time, uncorrelated between detectors, and uncorrelated with and much greater in power than the stochastic gravitational wave signal. Under these assumptions the expected variance, $\sigma_{Y_t}^2$, of the cross correlation is dominated by the noise in the individual detectors, whereas the expected value of the cross correlation Y_t depends on the stochastic background power spectrum:

$$\sigma_{Y_t}^2 \equiv \langle Y_t^2 \rangle - \langle Y_t \rangle^2 \approx \frac{T}{4}(Q_t, Q_t) \qquad (6)$$

$$\langle Y_t \rangle = T\left(Q_t, \frac{\int_{S^2} d\hat{\Omega}\, \gamma_{\hat{\Omega},t} P(\hat{\Omega}) H}{P_1 P_2}\right). \qquad (7)$$

Here the scalar product $(\cdot, \cdot)$ is defined as $(A, B) = \int_{-\infty}^{\infty} A^*(f) B(f) P_1(f) P_2(f) df$ and T is the duration of the measurement.

Equation (2) defines the optimal filter Q_t for any arbitrary choice of $P(\hat{\Omega})$. To optimize the method for finite, but unresolved astrophysical sources one should use a $P(\hat{\Omega})$ that covers only a localized patch in the sky. But the diffraction limit θ of two detectors separated by $d = 3000$ km is given by

$$\theta = \frac{c}{2fd} \approx \frac{50 \text{ Hz}}{f}. \qquad (8)$$

The relevant frequency depends on the assumed source power spectrum $H(f)$ as well as on the noise power spectra P_1 and P_2, but for a typical frequency f of 300 Hz θ is about 10°. Thus astrophysical sources will not be spatially resolved and we can choose to optimize the method for true point sources, i.e., $P(\hat{\Omega}) = \delta^2(\hat{\Omega}, \hat{\Omega}')$, which also allows for a more efficient implementation (see [6]).

We defined the strain power spectrum $H(f)$ of a point source as one-sided (positive frequencies only) and included the power in both polarizations. Thus $H(f)$ is related to the gravitational wave energy flux F_{GW} through

$$F_{\text{GW}} = \int_{f_{\min}}^{f_{\max}} F(f) df = \frac{c^3 \pi}{4G} \int_{f_{\min}}^{f_{\max}} H(f) f^2 df, \qquad (9)$$

with $F(f)$ the gravitational wave energy flux per unit frequency, c the light speed, and G Newton's constant. We look for strain power spectra $H(f)$ in the form of a power law with exponent β. The amplitude at the pivot point of 100 Hz is described by H_β, i.e.,

$$H(f) = H_\beta \left(\frac{f}{100 \text{ Hz}}\right)^\beta. \qquad (10)$$

With this definition we can choose the normalization of the optimal filter Q_t such that Eq. (7) reduces to

$$\langle Y_t \rangle = H_\beta. \qquad (11)$$

The data set from a given interferometer pair is divided into equal-length intervals, and the cross correlation Y_t and theoretical σ_{Y_t} are calculated for each interval, yielding a set $\{Y_t, \sigma_{Y_t}\}$ of such values for each sky direction $\hat{\Omega}$, with t labeling the intervals. The optimal filter Q_t is kept constant and equal to its midinterval value for the whole interval. The remaining error due to this discretization is of second order in $(T_{\text{seg}}/1 \text{ day})$ and is given by

$$Y_{\text{err}}(T_{\text{seg}})/Y = \frac{T_{\text{seg}}^2}{24} \frac{\int_{-\infty}^{\infty} (\partial^2 \gamma_{\hat{\Omega}'}^* / \partial t^2) \gamma_{\hat{\Omega}'} H^2 P_1^{-1} P_2^{-1} df}{\int_{-\infty}^{\infty} |\gamma_{\hat{\Omega}'}|^2 H^2 P_1^{-1} P_2^{-1} df}$$
$$= O\left(\left(\frac{2\pi f d}{c} \frac{T_{\text{seg}}}{1 \text{ day}}\right)^2\right) \qquad (12)$$

with f the typical frequency and d the detector separation. At the same time the interval length can be chosen such that the detector noise is relatively stationary over one interval. We use an interval length of 60 sec, which guarantees that the relative error $Y_{\text{err}}(T_{\text{seg}})/Y$ is less than 1%. The cross correlation values are combined to produce a final cross correlation estimator, Y_{opt}, that maximizes the signal-to-noise ratio, and has variance σ_{opt}^2:

$$Y_{\text{opt}} = \sum_t \sigma_{Y_t}^{-2} Y_t / \sigma_{\text{opt}}^{-2}, \qquad \sigma_{\text{opt}}^{-2} = \sum_t \sigma_{Y_t}^{-2}. \qquad (13)$$

In practice the intervals are overlapping by 50% to avoid the effective loss of half the data due to the required windowing (Hanning). Thus Eq. (13) was modified slightly to take the correlation of neighboring intervals into account.

The data was downsampled to 4096 Hz and high-pass filtered with a sixth order Butterworth filter with a cutoff frequency at 40 Hz. Frequencies between 50 and 1800 Hz were used for the analysis and the frequency bin width was 0.25 Hz. Frequency bins around multiples of 60 Hz up to the tenth harmonic were removed, along with bins near a set of nearly monochromatic injected signals used to simulate pulsars. These artificial pulsars proved useful in a separate end-to-end check of this analysis pipeline, which successfully recovered the sky locations, frequencies, and strengths of three such pulsars listed in Table I. The resulting map for one of these pulsars is shown in Fig. 1.

TABLE I. Injected pulsars: The table shows the level at which the three strongest injected pulsars were recovered. Hdf denotes the rms strain power over the 0.5 Hz band that was used. The reported values for the injected Hdf include corrections that account for the difference between the polarized pulsar injection and an unpolarized source that is expected by the analysis. The one sigma uncertainty in the recovered Hdf is given in row two (Noise level), and the ratio between recovered Hdf and noise level is given in row five (SNR). The significant underestimate of pulsar No. 4 is due to a known bias of the analysis method in the case of a signal strong enough to affect the power spectrum estimation.

| Injected pulsars Quantity	Pulsar No. 3	Pulsar No. 4	Pulsar No. 8
Frequency during S4 run	108.86 Hz	1402.20 Hz	193.94 Hz
Noise level (σ)	1.89×10^{-47}	6.04×10^{-46}	1.73×10^{-47}
Injected Hdf (corrected for polarization)	1.74×10^{-46}	4.28×10^{-44}	1.54×10^{-46}
Recovered Hdf on source	1.74×10^{-46}	4.05×10^{-44}	1.79×10^{-46}
Signal-to-noise ratio (SNR)	9.2	67.1	10.3
Injected position	11 h 53 m 29.4 s $-33° 26' 11.8''$	18 h 39 m 57.0 s $-12 °27' 59.8''$	23 h 25 m 33.5 s $-33 °25' 6.7''$
Recovered position (max SNR)	12 h 12 m $-37°$	18 h 40 m $-13°$	23 h 16 m $-32°$
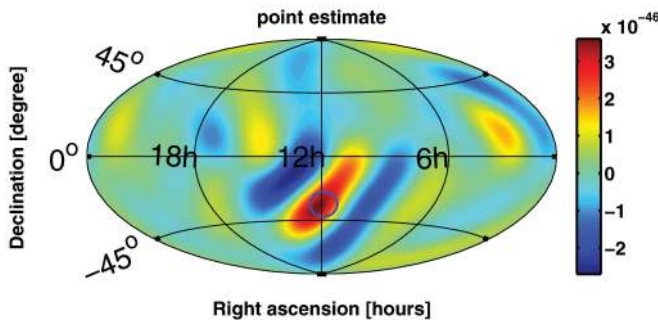
FIG. 1 (color). Injected pulsar No. 3: The analysis was run using the 108.625 Hz–109.125 Hz frequency band. The artificial signal of pulsar No. 3 at 108.86 Hz stands out with a signal-to-noise ratio of 9.2. The circle marks the position of the simulated pulsar.

III. LIGO S4 SCIENCE RUN

The LIGO S4 science run consisted of one month of coincident data taking with all three LIGO interferometers (22 February, 2005 noon to 23 March, 2005 midnight CST). During that time all three interferometers where roughly a factor of 2 in amplitude away from design sensitivity over almost the whole frequency band. Also, the Livingston interferometer was equipped with a hydraulic external preisolation (HEPI) system, allowing it to stay locked during daytime. This made S4 the first LIGO science run with all-day coverage at both sites. A more detailed description of the LIGO interferometers is given in [8].

Since the radiometer analysis requires two spatially separated sites we used only data from the two 4 km interferometers (H1 in Hanford and L1 in Livingston). For these two interferometers about 20 days of coincident data was collected, corresponding to a duty factor of 69%.

The large spatial separation also reduces environmental correlations between the two sites. Nevertheless we still found a comb of 1 Hz harmonics that was coherent between H1 and L1. This correlation was found to be at least in part due to an exactly 1-sec periodic signal in both interferometers (Fig. 2), which was caused by cross talk from the GPS_RAMP signal. The GPS_RAMP signal consists of a sawtooth signal that starts at every full second, lasts for 1 msec, and is synchronized with the GPS receivers (see Fig. 2). This ramp was used as an off-line monitor of the analog-to-digital converter (ADC) card timing and thus was connected to the same ADC card that was used for the gravitational wave channel, which resulted in a nonzero cross talk to the gravitational wave channel.

To reduce the contamination from this signal a transient template was subtracted in the time domain. This has the advantage that effectively only a very narrow band (1/run time $\approx 1 \times 10^{-6}$ Hz) is removed around each 1 Hz harmonic, while the rest of the analysis is unaffected. The waveform for subtraction from the raw (uncalibrated) data was recovered by averaging the data from the whole run in order to produce a typical second. Additionally, since this typical second only showed significant features in the first 80 msec, the transient subtraction template was set to zero (with a smooth transition) after 120 msec. This subtraction was done for only H1 since adding repetitive data to both detectors can introduce an artificial correlation. It eliminated the observed correlation. However, due to an automatically adjusted gain between the ADC card and the gravitational wave channel, the amplitude of the transient waveform is affected by a residual systematic error. Its effect on the cross correlation result was estimated by comparing maps with the subtraction done on either H1 or L1. The systematic error is mostly concentrated around the North and South Poles, with a maximum of about 50% of the statistical error at the South Pole. In the declination
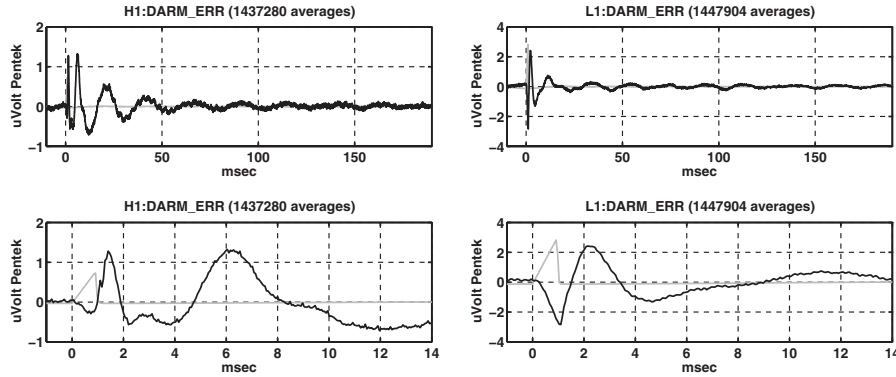
FIG. 2.   Periodic timing transient in the gravitational wave channel (DARM_ERR), calibrated in μV at the ADC (Pentek card) for H1 (left two graphs) and L1 (right two graphs) shown with a span of 200 and 14 msec in black. The x axis is the offset from a full GPS second. About 1.4×10^6 sec of DARM_ERR data was averaged to get this trace. Also shown in gray is the GPS_RAMP signal that was used as a timing monitor. It was identified as a cause of the periodic timing transient in DARM_ERR. The H1 trace shows an additional feature at 6 msec.

range of $-75°$ to $+75°$ the error is less than 10% of the statistical error. For upper limit calculations this systematic error is added in quadrature to the statistical error. After the S4 run the GPS_RAMP signal was replaced with a two-tone signal at 900 and 901 Hz. The beat between the two is now used to monitor the timing.

One postprocessing cut was required to deal with detector nonstationarity. To avoid a bias in the cross correlation statistics the interval before and the interval after the one being analyzed are used for the power spectral density (PSD) estimate [9]. Therefore the analysis becomes vulnerable to large, short transients that happen in one instrument in the middle interval—such transients cause a significant underestimate of the PSD and thus of the theoretical standard deviation for this interval. This leads to a contamination of the final estimate.

To eliminate this problem the standard deviation σ is estimated for both the middle interval and the two adjacent intervals. The two estimates are then required to agree within 20%:

$$\frac{1}{1.2} < \frac{\sigma_{\text{middle}}}{\sigma_{\text{adjacent}}} < 1.2. \quad (14)$$

The analysis is fairly insensitive to the threshold—the only significant contamination comes from very large outliers that are cut by any reasonable threshold [10]. The chosen threshold of 20% eliminates less than 6% of the data.

IV. RESULTS FROM THE S4 RUN

A. Broadband results

In this analysis we searched for an $H(f)$ following a power law with two different exponents β.
  (i) $\beta = -3$: $H(f) = H_{-3}(100 \text{ Hz}/f)^3$.
      This emphasizes low frequencies and is useful when interpreting the result in a cosmological framework, since it corresponds to a scale-invariant primordial

perturbation spectrum, i.e., the GW energy per logarithmic frequency interval is constant.
  (ii) $\beta = 0$: $H(f) = H_0$ *(constant strain power)*.
      This emphasizes the frequencies for which the interferometer strain sensitivity is highest.

The results are reported as point estimate $Y_{\hat{\Omega}}$ and corresponding standard deviation $\sigma_{\hat{\Omega}}$ for each pixel $\hat{\Omega}$. The point estimate $Y_{\hat{\Omega}}$ must be interpreted as best fit amplitude H_β for the pixel $\hat{\Omega}$ [Eq. (11)].

Also we should note that the resulting maps have an intrinsic spatial correlation, which is described by the point spread function

$$A(\hat{\Omega}, \hat{\Omega}') = \frac{\langle Y_{\hat{\Omega}} Y_{\hat{\Omega}'} \rangle}{\langle Y_{\hat{\Omega}'} Y_{\hat{\Omega}'} \rangle}. \quad (15)$$

It describes the spatial correlation in the following sense: if either $Y_{\hat{\Omega}'} = \bar{Y}$ due to random fluctuations, or if there is a true source of strength $\bar{Y}$ at $\hat{\Omega}'$, then the expectation value at $\hat{\Omega}$ is $\langle Y_{\hat{\Omega}} \rangle = A(\hat{\Omega}, \hat{\Omega}') \bar{Y}$. The shape of $A(\hat{\Omega}, \hat{\Omega}')$ depends strongly on the declination. Figure 3 shows $A(\hat{\Omega}, \hat{\Omega}')$ for different source declinations and both the $\beta = -3$ and $\beta = 0$ case, assuming continuous day coverage.

1. Scale-invariant case, $\beta = -3$

A histogram of the SNR $= Y/\sigma$ (SNR, signal-to-noise ratio) is plotted in Fig. 4. The data points were weighted with the corresponding sky area in square degrees. Because neighboring points are correlated, the effective number of independent points N_{eff} is reduced. Therefore the histogram can exhibit statistical fluctuations that are significantly larger than those naively expected from simply counting the number of pixels in the map, while still being consistent with (correlated) Gaussian noise. Indeed the histogram in Fig. 4 features a slight bump around SNR $= 2$, but is still consistent with $N_{\text{eff}} = 100$—the dash-dotted lines indicate the one sigma band around the ideal
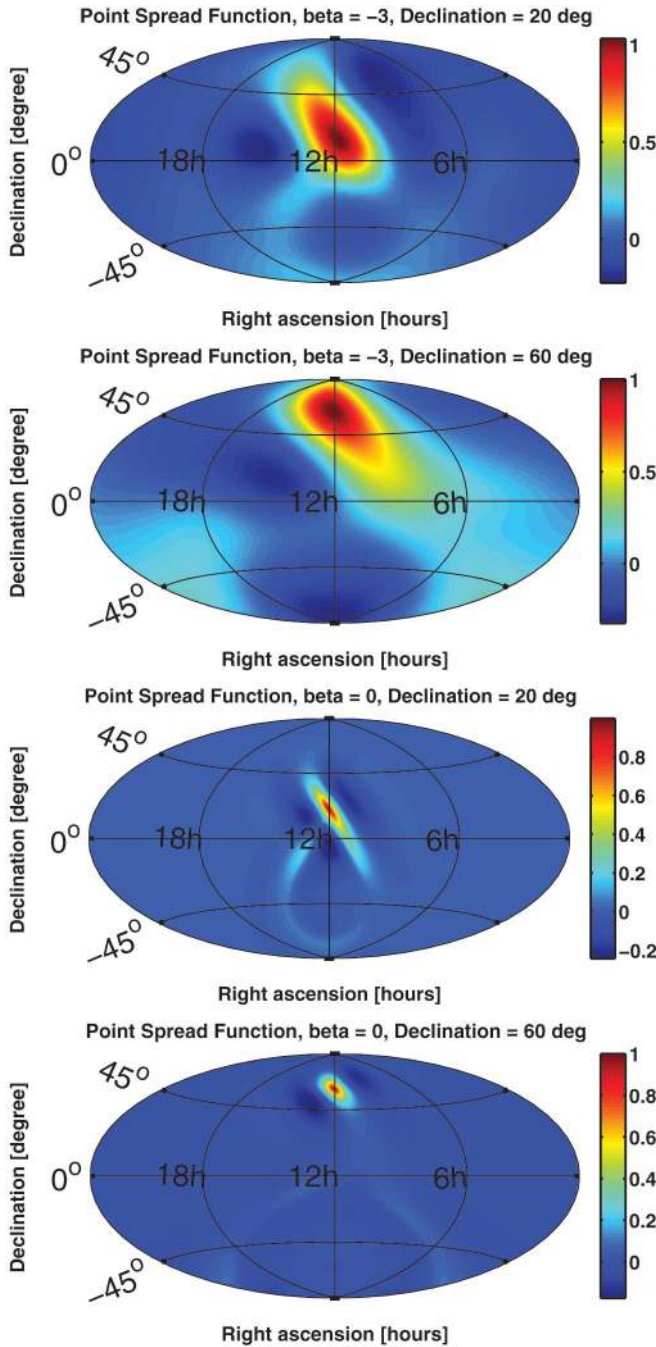
FIG. 3 (color).   Point spread function $A(\hat{\Omega}, \hat{\Omega}')$ of the radiometer for $\beta = -3$ (top two figures) and for $\beta = 0$ (bottom two figures). Plotted is the relative expected signal strength assuming a source at right ascension 12 h and declinations 20° and 60°. Uniform day coverage was assumed, so the resulting shapes are independent of right ascension. An Aitoff projection was used to plot the whole sky.

Gaussian for $N_{eff} = 100$. Additionally the SNR distribution also passes a Kolmogorov-Smirnov test for $N_{eff} = 100$ at the 90% significance level.

The number of independent points N_{eff}, which in effect describes the diffraction limit of the LIGO detector pair,

was estimated by 2 heuristic methods.

(i) *Spherical harmonics decomposition* of the SNR map. The resulting power versus l graph shows structure up to roughly $l = 9$ and falls off steeply above that—the $l = 9$ point corresponds to one twentieth of the maximal power. The effective number of independent points then is $N_{eff} \approx (l + 1)^2 = 100$.

(ii) *FWHM area* of a strong injected source, which is latitude dependent but of the order of 800 square degrees. To fill the sky we need about $N_{eff} \approx 50$ of those patches. We used the higher estimate $N_{eff} = 100$ for this discussion.

Figure 4 suggests that the data are consistent with no signal. Thus we calculated a Bayesian 90% upper limit for each sky direction. The prior was assumed to be flat between zero and an upper cutoff set to 5×10^{-45} Hz^{-1} at 100 Hz, the approximate limit that can be set from just operating a single LIGO interferometer at the S4 sensitivity. Note, however, that this cutoff is so high that the upper limit is completely insensitive to it. Additionally we marginalized over the calibration uncertainty of 8% for H1 and 5% for L1 using a Gaussian probability distribution. The resulting upper limit map is shown in Fig. 5. The upper limits on the strain power spectrum $H(f)$ vary between 1.2×10^{-48} Hz^{-1} $(100$ Hz$/f)^3$ and 1.2×10^{-47} Hz^{-1} $(100$ Hz$/f)^3$, depending on the position in the sky. These strain limits correspond to limits on the gravitational wave energy flux per unit frequency $F(f)$ varying between 3.8×10^{-6} erg cm^{-2} Hz^{-1} $(100$ Hz$/f)$ and 3.8×10^{-5} erg cm^{-2} Hz^{-1} $(100$ Hz$/f)$.
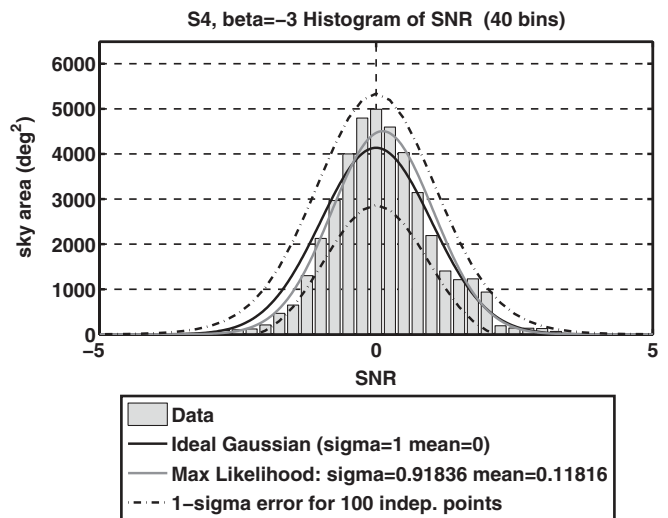

FIG. 4.   S4 Result: Histogram of the signal-to-noise ratio (SNR) for $\beta = -3$. The gray curve is a maximum likelihood Gaussian fit to the data. The black solid line is an ideal Gaussian, the two dash-dotted black lines indicate the expected one sigma variations around this ideal Gaussian for 100 independent points ($N_{eff} = 100$).
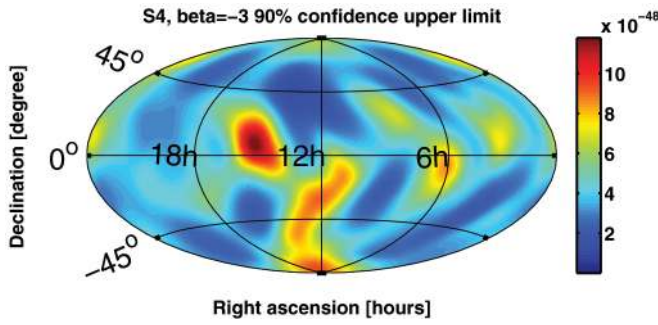
FIG. 5 (color). S4 Result: Map of the 90% confidence level Bayesian upper limit on H_β for $\beta = -3$. The upper limit varies between 1.2×10^{-48} Hz^{-1} (100 Hz/f)^3 and 1.2×10^{-47} Hz^{-1} (100 Hz/f)^3, depending on the position in the sky. All fluctuations are consistent with the expected noise.
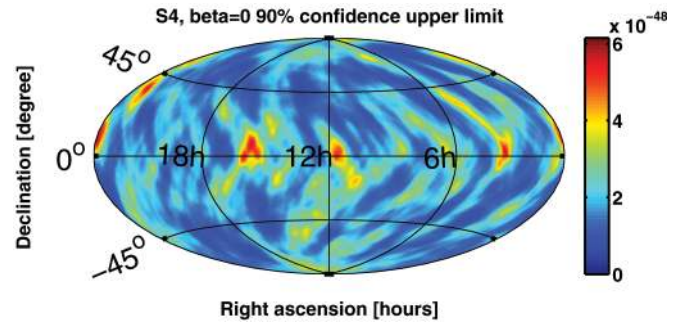

FIG. 7 (color). S4 Result: Map of the 90% confidence level Bayesian upper limit on H_β for $\beta = 0$. The upper limit varies between 8.5×10^{-49} Hz^{-1} and 6.1×10^{-48} Hz^{-1} depending on the position in the sky.

2. Constant strain power, $\beta = 0$

Similarly, Fig. 6 shows a histogram of the SNR $= Y/\sigma$ for the constant strain power case. Structure in the spherical harmonics power spectrum goes up to $l = 19$, thus $N_{\rm eff}$ was estimated to be $N_{\rm eff} \approx (l + 1)^2 = 400$. Alternatively the FWHM area of a strong injection covers about $100°^2$ which also leads to $N_{\rm eff} \approx 400$. The dash-dotted lines in the histogram (Fig. 6) correspond to the expected one sigma deviations from the ideal Gaussian for $N_{\rm eff} = 400$. The histogram is thus consistent with (correlated) Gaussian noise, indicating that there is no signal present. The SNR distribution also passes a Kolmogorov-Smirnov test for $N_{\rm eff} = 400$ at the 90% significance level.

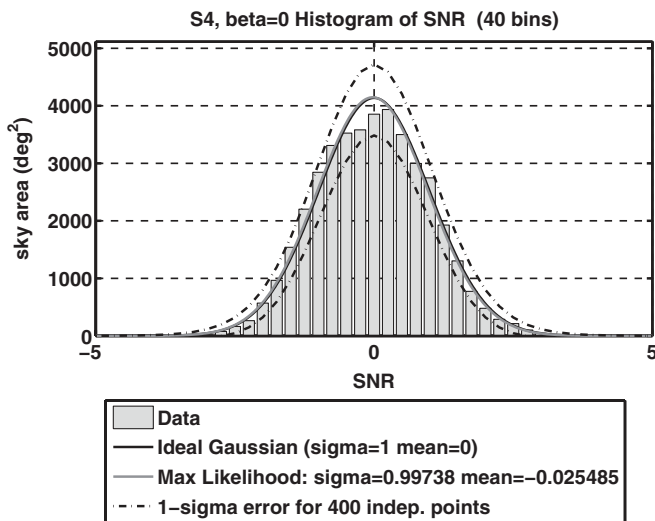Again we calculated a Bayesian 90% upper limit for each sky direction, including the marginalization over the

calibration uncertainty. The prior was again assumed to be flat between 0 and an upper cutoff of 5×10^{-45} Hz^{-1} at 100 Hz. The resulting upper limit map is shown in Fig. 7. The upper limits on the strain power spectrum $H(f)$ vary between 8.5×10^{-49} Hz^{-1} and 6.1×10^{-48} Hz^{-1} depending on the position in the sky. This corresponds to limits on the gravitational wave energy flux per unit frequency $F(f)$ varying between 2.7×10^{-6} erg cm^{-2} Hz^{-1} (f/100 Hz)^2 and 1.9×10^{-5} erg cm^{-2} Hz^{-1} (f/100 Hz)^2.

3. Interpretation

The maps presented in Figs. 5 and 7 represent the first directional upper limits on a stochastic gravitational wave background ever obtained. They are consistent with no gravitational wave background being present. This search is optimized for well localized, broadband sources of gravitational waves. As such it is best suited for unexpected, poorly modeled sources.

In order to compare the result to what could be expected from known sources we also search for the gravitational radiation from low-mass x-ray binaries (LMXBs). They are accretion-driven spinning neutron stars, i.e., narrow band sources and thus not ideal for this broadband search. However they have the advantage that we can predict the gravitational wave energy flux based on the known x-ray flux. If gravitational radiation provides the torque balance for LMXBs, then there is a simple relation between the gravitational wave energy flux $F_{\rm GW}$ and x-ray flux F_X [11]:

$$F_{\rm GW} \approx \frac{f_{\rm spin}}{f_{\rm Kepler}} F_X. \qquad (16)$$

Here $f_{\rm Kepler}$ is final orbital frequency of the accreting matter, about 2 kHz for a neutron star, and $f_{\rm spin}$ is spin frequency.

As an example we estimate the gravitational wave energy flux of all LMXBs within the Virgo galaxy cluster. Their integrated x-ray flux is about 10^{-9} erg/ sec /cm^2 (3000 galaxies at 15 Mpc, 10^{40} erg/ sec /galaxy from

FIG. 6. S4 Result: Histogram of the SNR for $\beta = 0$. The gray curve is a maximum likelihood Gaussian fit to the data. The black solid line is an ideal Gaussian, the two dash-dotted black lines indicate the expected one sigma variations around this ideal Gaussian for 400 independent points ($N_{\rm eff} = 400$).

LMXBs). For simplicity we assume that the ensemble produces a flat strain power spectrum $H(f)$ over a bandwidth Δf. Then the strength of this strain power spectrum is about

$$H(f) = \frac{2G}{\pi c^3} \frac{1}{f_{\text{Kepler}} f_{\text{center}} \Delta f} F_X$$

$$\approx 10^{-55} \text{ Hz}^{-1} \left(\frac{100 \text{ Hz}}{f_{\text{center}}}\right)\left(\frac{100 \text{ Hz}}{\Delta f}\right). \qquad (17)$$

Here f_{center} is the typical frequency of the Δf wide band of interest. This is quite a bit weaker than the upper limit set in this paper, which is mostly due to the fact that the intrinsically narrow band sources are diluted over a broad frequency band.

B. Limits on isotropic background

It is possible to recover the estimate for an isotropic background as an integral over the map (see [6]). The corresponding theoretical standard deviation would require a double integral with essentially the point spread function as integrand. In practice it is simpler to calculate this theoretical standard deviation directly by using the overlap reduction function for an isotropic background (see [7]). From that the 90% Bayesian upper limit can be calculated, which is additionally marginalized over the calibration uncertainty.

Limits on an isotropic background of gravitational waves are traditionally quoted as either the strain power spectrum $S_{\text{GW}}(f)$ seen by an interferometer, or as $\Omega_{\text{GW}}(f)$, the GW energy density per unit logarithmic frequency, divided by the critical energy density ρ_c to close the Universe. They are related to $H(f)$ by

$$\Omega_{\text{GW}}(f) = \frac{10\pi^2}{3H_0^2} f^3 S_{\text{Gw}}(f) = \frac{8\pi^3}{3H_0^2} f^3 H(f). \qquad (18)$$

Here $H_0 = 72 \text{ km sec}^{-1} \text{Mpc}^{-1}$ is the Hubble constant today. We again assume a power law for these quantities,

$$S_{\text{GW}}(f) = S_{\text{GW},\beta}\left(\frac{f}{100 \text{ Hz}}\right)^{\beta}$$

$$\Omega_{\text{GW}}(f) = \Omega_{\text{GW},\beta}\left(\frac{f}{100 \text{ Hz}}\right)^{\beta+3}, \qquad (19)$$

and set a limit on their amplitude. For the scale-invariant case $\beta = -3$ we can set a 90% upper limit of 1.20×10^{-4} on $\Omega_{\text{GW},-3}$. Table II summarizes the results for both choices of β.

Interpretation

In [3] we published an upper limit of $\Omega_{\text{GW}} < 6.5 \times 10^{-5}$ on an isotropic gravitational wave background using S4 data. That analysis is mathematically identical to inferring the point estimate as an integral over the map [6], but the mitigation of the timing transient and the data quality cuts were sufficiently different to affect the point estimate. While both results are consistent within the error bar of the measurement, this difference results in a slightly higher upper limit. Both results are significantly better than the previously published LIGO S3 result.

C. Narrow band results targeted on Sco-X1

As an application we again focus on LMXBs. The gravitational wave flux from all LMXBs is expected to be dominated by the brightest one, Sco-X1, simply because Sco-X1 dominates the x-ray flux from all LMXBs, and x-ray flux F_X is related to the gravitational wave energy flux F_{GW} through Eq. (16). Unfortunately the spin frequency of Sco-X1 is not known. We thus want to set an upper limit for each frequency bin on the rms strain coming from the direction of Sco-X1 (right ascension: 16 h 19 m 55.0850 s; declination: $-15\,°38'\,24.9''$).

The binary orbital velocity of Sco-X1 is about $40 \pm 5 \text{ km/sec}$ (see [12]). This induces a maximal frequency shift of $\Delta f_{\text{GW}} = 2.7 \times 10^{-4} \times f_{\text{GW}}$. We chose a bin width of $df = 0.25 \text{ Hz}$, which is broader than maximal frequency shift Δf_{GW} for all frequencies below 926 Hz and is the same bin width that was used for the broadband

TABLE II. S4 isotropic result for the $\Omega_{\text{GW}}(f) = \text{const}$, $(\beta = -3)$ and the $S_{\text{GW}}(f) = \text{const}$, $(\beta = 0)$ case. The first two lines show the point estimate and standard deviation that are used to calculate the 90% Bayesian upper limits. The upper limits (UL) are also marginalized over the calibration uncertainty. These results agree with the ones published in [3] within the error bar of the measurement.

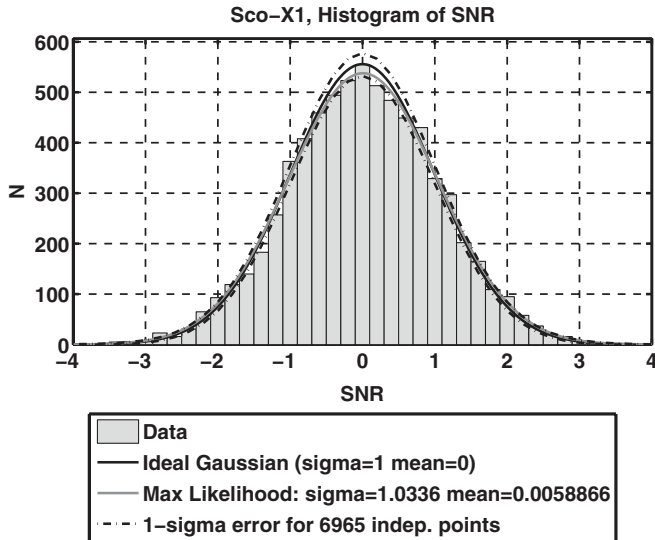| S4 isotropic upper limit	Power law	
Quantity	$\beta = -3$	$\beta = 0$
Point estimate for $S_{\text{GW},\beta}$	$1.02 \times 10^{-47} \text{ Hz}^{-1}$	$-7.12 \times 10^{-48} \text{ Hz}^{-1}$
Corresponding standard deviation	$6.97 \times 10^{-48} \text{ Hz}^{-1}$	$7.22 \times 10^{-48} \text{ Hz}^{-1}$
90% Bayesian UL on $S_{\text{GW},\beta}$	$1.99 \times 10^{-47} \text{ Hz}^{-1}$	$8.49 \times 10^{-48} \text{ Hz}^{-1}$
90% Bayesian UL on $\Omega_{\text{GW},\beta}$	1.20×10^{-4}	5.13×10^{-5}

FIG. 8. S4 Result for Sco-X1: Histogram of the signal-to-noise ratio calculated for each 0.25 Hz wide frequency bin. There are no outliers.

analysis. Above 926 Hz the signal is guaranteed to spread over multiple bins.

To avoid contamination from the hardware-injected pulsars, the 2 frequency bins closest to a pulsar frequency were excluded. Multiples of 60 Hz were also excluded. The lowest frequency bin was at 50 Hz, the highest one at 1799.75 Hz. Figure 8 shows a histogram of the remaining 6965 0.25 Hz wide frequency bins. It is consistent with a Gaussian distribution (Kolmogorov-Smirnov test with $N = 6965$ at the 90% significance level).
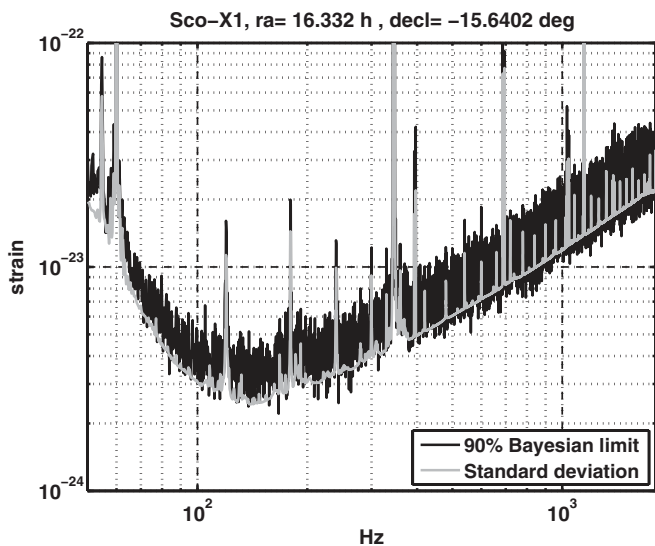

FIG. 9. S4 Result for Sco-X1: The 90% confidence Bayesian upper limit as a function of frequency—marginalized over the calibration uncertainty. The standard deviation (one sigma error bar) is shown in gray.

A 90% Bayesian upper limit for each frequency bin was calculated based on the point estimate and standard deviation, including a marginalization over the calibration uncertainty. Figure 9 is a plot of this 90% limit (black trace). Above about 200 Hz (shot noise regime above the cavity pole) the typical upper limit rises linearly with frequency and is given by

$$h_{\mathrm{rms}}^{(90\%)} \approx 3.4 \times 10^{-24}\left(\frac{f}{200\ \mathrm{Hz}}\right), \qquad f \gtrsim 200\ \mathrm{Hz}. \quad (20)$$

The standard deviation is also shown in gray.

Interpretation

In principle, the radiometer analysis is not an optimal method to search for a presumably periodic source like Sco-X1. Nevertheless it can set a competitive upper limit with a minimal set of assumptions on the source and significantly less computational resources. Indeed LIGO published a 95% upper limit on gravitational radiation amplitude from Sco-X1 of 1.7×10^{-22} to 1.3×10^{-21} across the 464–484 Hz and 604–624 Hz frequency bands [13], using data from S2, which had a noise amplitude about 4.5 times higher around 500 Hz in each instrument. The analysis was computationally limited to using 6 h of data and two 20 Hz frequency bands. However the strain amplitude sensitivity of the radiometer analysis scales as $T^{-1/4}$ [6], while a coherent method scales as $T^{-1/2}$.

The upper limit [Eq. (20)] can directly be compared to the expected strain based on the x-ray flux:

$$\frac{h_{\mathrm{rms}}^{(90\%)}}{h_{\mathrm{rms}}^{L_x}} \approx 100\left(\frac{f}{200\ \mathrm{Hz}}\right)^{3/2}, \qquad f \gtrsim 200\ \mathrm{Hz}. \quad (21)$$

Here f is the gravitational wave frequency, i.e., twice the (unknown) spin frequency of Sco-X1. This is close enough that, if the model described in [11], and thus Eq. (16) are indeed correct, Sco-X1 ought to be detectable with this method and the next generation of gravitational wave detectors operated in a narrow band configuration (AdvLIGO [14]). For a discussion of the expected signal from Sco-X1 see also [13].

V. CONCLUSION

We produced the first upper limit maps for a stochastic gravitational wave background by applying a method that is described in [6] to the data from the LIGO S4 science run. No signal was seen and upper limits were set for two different choices for the strain power spectrum $H(f)$. In the case of $H(f) \propto f^{-3}$ the upper limits for a point source vary between 1.2×10^{-48} Hz^{-1} (100 Hz/f)^3 and 1.2×10^{-47} Hz^{-1} (100 Hz/f)^3, depending on the position in the sky (see Fig. 5). Similarly, in the case of constant $H(f)$ the upper limits vary between 8.5×10^{-49} Hz^{-1} and 6.1×10^{-48} Hz^{-1} (see Fig. 7). As a side product limits on an

isotropic background of gravitational waves were also obtained, see Table II.

In an additional application, narrow band upper limits were set on the gravitational radiation coming from the brightest low-mass x-ray binary, Sco-X1 (see Fig. 9). In the shot noise limited frequency band (above about 200 Hz) the limits on the strain in each 0.25 Hz wide frequency bin follow roughly

$$h_{\mathrm{rms}}^{(90\%)} \approx 3.4 \times 10^{-24} \left(\frac{f}{200 \text{ Hz}} \right), \qquad f \gtrsim 200 \text{ Hz}, \quad (22)$$

where f is the gravitational wave frequency (twice the spin frequency).

ACKNOWLEDGMENTS

[1] L. Bildsten, Astrophys. J. **501**, L89 (1998)
[2] T. Regimbau and J. A. de Freitas Pacheco Astron. Astrophys. **376**, 381 (2001).
[3] B. Abbott *et al.*, Astrophys. J. **659**, 918 (2007).
[4] B. Abbott *et al.*, Phys. Rev. Lett. **95**, 221101 (2005).
[5] B. Abbott *et al.*, Phys. Rev. D **69**, 122004 (2004).
[6] S. W. Ballmer, Classical Quantum Gravity **23**, S179 (2006).
[7] B. Allen and J. D. Romano, Phys. Rev. D **59**, 102001 (1999).
[8] B. Abbott *et al.*, Nucl. Instrum. Methods Phys. Res., Sect. A **517**, 154 (2004).
[9] A. Lazzarini and J. Romano, http://www.ligo.caltech.edu/docs/T/T040089-00.pdf.
[10] S. W. Ballmer, Ph.D. thesis, Massachusetts Institute of Technology (MIT), 2006.
[11] R. V. Wagoner, Astrophys. J. **278**, 345 (1984).
[12] D. Steeghs and J. Cesares, Astrophys. J. **568**, 273 (2002).
[13] B. Abbott *et al.*, arXiv:gr-qc/0605028 [Phys. Rev. D (to be published)].
[14] http://www.ligo.caltech.edu/advLIGO/.